OPEN ACCESS
IOP Publishing | International Atomic Energy Agency
Nuclear Fusion
Nucl. Fusion **63** (2023) 036002 (8pp)
https://doi.org/10.1088/1741-4326/acb21f

Impact of β_n and spectrum of $n = 1$ applied fields on fast ion losses in DIII-D

K.R. Gage[1,*], X. Chen[2], M. Van Zeeland[2], W.W. Heidbrink[1], J. Hanson[3], B. Lyons[2], D.C. Pace[2], J. Galdon-Quiroga[4,5] and M. Garcia-Munoz[4]

[1] University of California, Irvine, CA, United States of America
[2] General Atomics, San Diego, CA, United States of America
[3] Columbia University, New York, NY, United States of America
[4] University of Seville, Seville, Spain
[5] Max Planck Institute for Plasma Physics, Garching, Germany

E-mail: gagek@uci.edu

Received 21 September 2022, revised 9 December 2022
Accepted for publication 11 January 2023
Published 25 January 2023

Abstract

The effect of $n = 1$ magnetic perturbations (MPs) on prompt fast ion losses in DIII-D has been investigated using the light ion beam probe technique. The effect of normalized beta, β_n, and the plasma response to the MPs is studied for several MP spectra. Magnetics data show a strong dependence of plasma response to β_n that depends on the phase difference in perturbation coils, $\Delta\phi_{\mathrm{UL}}$. For most phases, the response increases with β_n, however, the response is suppressed for phases between 180° and 240°. Experimental data from scintillator based fast ion loss detectors shows that relative fluctuation of lost ions (20%–30% of the steady signal) does not diminish across the L- to H-mode transition for $\Delta\phi_{\mathrm{UL}} = 240°$, despite the 34% decrease in radial response field and 50% decrease in poloidal response field. Simulations of the DIII-D discharges using M3D-C1 and ASCOT5 find that prompt losses from neutral beam injection in each investigated case hit the first wall at several concentrated locations: the vessel floor, midplane diagnostic ports, vessel ceiling, and inner wall. Simulated losses from co-injection neutral beams are born outside the last closed flux surface, corresponding to radial orbit displacements of 3–6 cm due to the MPs.

Keywords: energetic particles, tokamaks, fast ion losses, magnetic perturbations

(Some figures may appear in colour only in the online journal)

1. Introduction

Ensuring that future fusion plasma devices will be able to survive H-mode plasmas is of great concern. Peak heat fluxes from Type I edge localized modes (ELMs) are expected to be unmanageable in devices such as SPARC [1], DEMO [2], and ITER [3]. Research into ELM suppression has included the use of externally applied resonant magnetic perturbations (MPs) to alter ELM stability [4]. Successful use of resonant MPs in mitigating and suppressing ELMs has been achieved on several devices, including DIII-D [5], AUG [6], EAST [7], and KSTAR [8].

These 3D field schemes have come at a cost, however, as MPs can lead to detrimental effects on both the edge and core, leading to issues such as loss of confinement [4, 9]. Furthermore, tokamaks around the world have reported fast ion losses induced by MPs [10–15]. Loss of energetic particles is, in general, problematic as it reduces the efficiency of heating from fusion born alphas and external heating schemes such

* Author to whom any correspondence should be addressed.

as neutral beam injection (NBI). Fast ion losses also present a potential issue for future devices in terms of heat flux to the first wall. This has prompted several studies of predicted heat fluxes in future devices [16–20].

Experiments and modeling of current devices are needed to learn how to simultaneously mitigate ELMs and fast ion losses. These cover a range of MP driven loss mechanisms including magnetic island transport [21], the importance of the plasma response [11, 21] to MPs, radial electric field effects [22], the orbits affected by MPs and how topological boundary crossing plays a role [23], how resonances between fast ions and the perturbations drive losses [24–26], and how the MP spectrum and toroidal phase change loss patterns [18, 26, 27].

The plasma response can have either a magnification or suppression effect on MPs. The resonant fields can be amplified based on the current stability to the resistive wall mode [28, 29], but the plasma response also tends to decrease magnetic island width in many cases [11, 26].

As the plasma response is related to β_n [29], this paper looks at a set of DIII-D discharges that covered a range of β_n values to modify the plasma response amplitudes. The effect on $n = 1$ MP induced losses over several magnetic spectra are analyzed to determine the radial displacement of lost fast ion orbits. Simulations of the discharges compare the effects of magnetic spectrum, β_n, and beam geometry on losses.

This paper is organized as follows: In section 2, we present the setup used for the experiments on DIII-D. The light ion beam probe (LIBP) technique [30] is explained. In section 3, we describe the results of experiments at DIII-D, most importantly the effect of β_n and the plasma response on fast ion losses. In section 4, we describe several ASCOT simulations and how the results compare with and elucidate our experimental results. Finally, in section 5, we summarize our conclusions.

2. Experimental setup

The MPs used in this work are generated by the DIII-D internal perturbation coils (I coils): two sets of six coils each, one above the midplane and one below as shown in figure 1(*b*). These coils can generate perturbations with toroidal mode numbers of up to $n = 3$, but here we will focus on $n = 1$ MPs. The I coils are also capable of having the upper and lower sets be energized independently, allowing for a toroidal phase difference, $\Delta\phi_{\mathrm{UL}}$, to separate the two coil sets. This $\Delta\phi_{\mathrm{UL}}$ can be held constant while the MP is rotated, allowing diagnostics to see the full perturbation.

Measurements of the plasma response to the MPs in this work utilize the midplane magnetic probes on DIII-D [31]. Both the radial and poloidal components of the plasma response can be measured using two separate probes as seen in figure 1(*b*). By selecting the component of the probe data with the frequency of the applied MP and removing the vacuum response to the I coils, the plasma response can be obtained as discussed in [32]. Figure 2 shows both the full magnetic fields measured as well as the resulting calculated plasma response levels to the rotating fields. This work also uses data from the two scintillator based fast ion loss detectors (FILDs) on DIII-D [33, 34]. These are marked in both their toroidal and poloidal locations in figure 1.

In order to directly relate the losses measured in the FILDs to the changes in the orbits of fast ions due to the applied MP, we use the LIBP technique [30, 35]. This requires that we have a neutral beam source that deposits ions into the plasma which are promptly lost to the FILD location. We ensure that the losses measured are first orbit losses by having periodic times with the beam power turned off for several milliseconds. The rotating MP then modulates the FILD signal according to the formula

$$\xi = \frac{\Delta F}{\bar{F}} L_i \tag{1}$$

where ξ is the radial displacement of an orbit due to the MP, ΔF is the amplitude of the FILD modulation, $\bar{F}$ is the average FILD prompt loss signal over the MP rotation period, and L_i is the ionization scale length where the lost particle was born. While the ionization scale length of the probing NBI source can be approximated by the electron density scale length, L_n, near the last closed flux surface (LCFS) [30], beam attenuation further inside the plasma leads to a significant change in density profiles a few centimeters away from the edge in both L-mode and H-mode. This can be seen in figure 3(*b*) where the simulated beam deposition profile is compared to the measured electron density. Here, the electron temperature and density are obtained from Thompson Scattering. The beam deposition is simulated using a Monte Carlo approach using the beam geometry and plasma profiles to determine the path length of neutrals through the plasma before they ionize. Figure 3(*b*) shows the histogram of particle markers normalized to the edge electron densities for comparison.

The experimental data for this work is taken from a database of shots on DIII-D. A sample discharge is shown in figure 4. Each shot began in L-mode and, after several MP rotation periods, was transitioned into H-mode to increase the normalized pressure β_n. The experiments ran at a toroidal magnetic field of 2 T, plasma current of 0.6–0.8 MA, and covered a range in β_n up to approximately 3.2. During the H-mode phase of these discharges, ELMs were not suppressed by the applied MPs. The $n = 1$ MPs were generated with five toroidal phase differences, $\Delta\phi_{\mathrm{UL}}$, of 0°, 120°, 180°, 240°, and 300°, with the 0° and 240° scenarios being explored more in-depth. The MPs were rigidly rotated at a frequency of 25 Hz. In order to maintain a consistent injected power from the probing beam, the transition to H-mode was triggered by adding in a separate NBI source. For nearly all cases, the probing beam was a co-current, tangentially injected beam with an injection energy of 81 keV; however, a counter-current beam was used for a single 240° L-mode case for a comparison of losses due to beam geometry. The plasma current, I_{p}, was also lowered during the H-mode transition to maintain alignment of the NBI prompt losses hitting the FILDs. This counteracted the change in current profile caused during the transition that would otherwise alter the precession of fast ions and cause them to be toroidally displaced from the detectors.

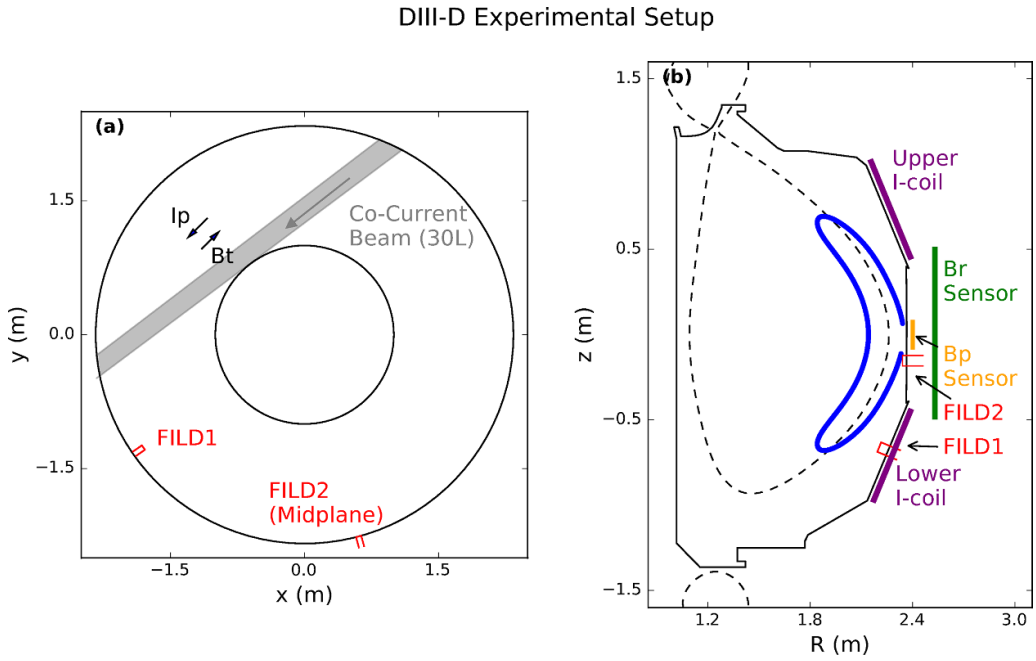

Figure 1. Top down (*a*) and poloidal cross-section (*b*) views of the DIII-D tokamak with experimental diagnostic locations highlighted. In (*b*), an example guiding center lost orbit is shown in blue.

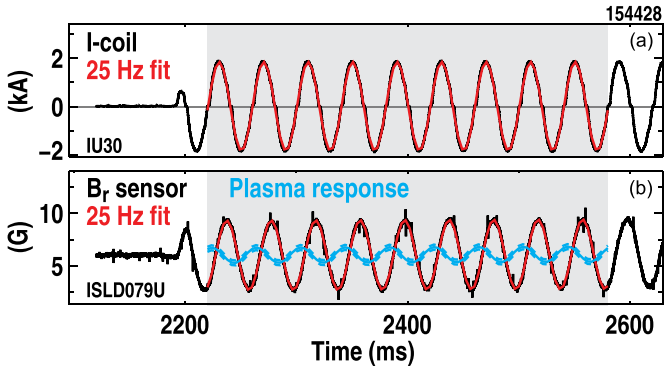

Figure 2. I Coil current (*a*) and magnetic probe data (*b*) during MP rotation. The plasma response after removal of the vacuum fields is shown in blue.

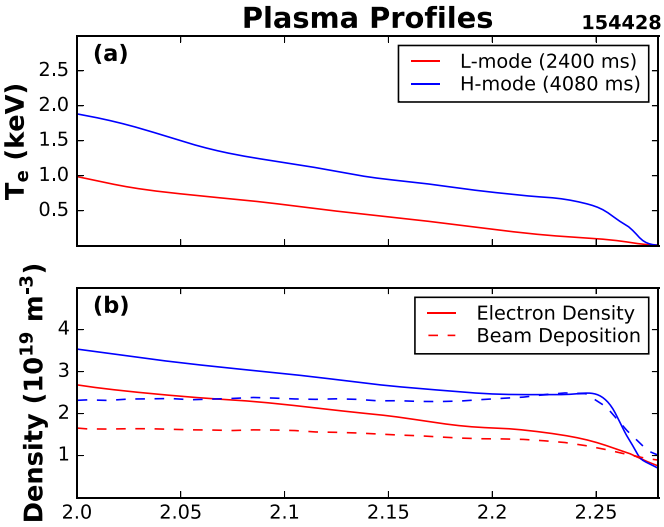

Figure 3. Edge temperature (*a*) and density (*b*) profiles inside the LCFS. In (*b*), simulated beam deposition profiles (dashed) are normalized to the electron density (solid) to show the effect of beam attenuation.

3. Experimental results

3.1. Plasma response measurements

Measurements of the plasma response to the applied MPs allow us to translate effects of β_n on the fast ion losses via its effect on the response amplitudes. Here, we use magnetics data over one to five MP rotation periods to determine the response levels. As shown in figure 5, an increase in β_n can lead to either a suppression or enhancement of the plasma response measured based on the MP spectrum. For both suppression and enhancement, the effect is most noticeable for $\beta_n > 1$ for nearly all $\Delta\phi_{\mathrm{UL}}$. Suppression is strongest in the $\Delta\phi_{\mathrm{UL}} = 240°$ case, but is also seen in the 180° discharges; however, the poloidal component of the response rises rapidly after $\beta_n \approx 2.4$ for the $\Delta\phi_{\mathrm{UL}} = 240°$ MPs. Only the fully out of phase perturbations lead to suppression of the poloidal field at highest β_n. This stark difference between the radial and poloidal components may be due to a high poloidal mode number of the perturbation. Since the radial field probe is large, it averages over a larger poloidal angle, where the poloidal probe acts more like a single point detector (see figure 1(*b*)).

3.2. Fast ion loss measurements

To examine the differences in losses between the two main MP spectra, $\Delta\phi_{\mathrm{UL}} = 0°$ and 240°, we fit sinusoidal waveforms to data taken via photomultiplier tubes (PMTs) observing fast

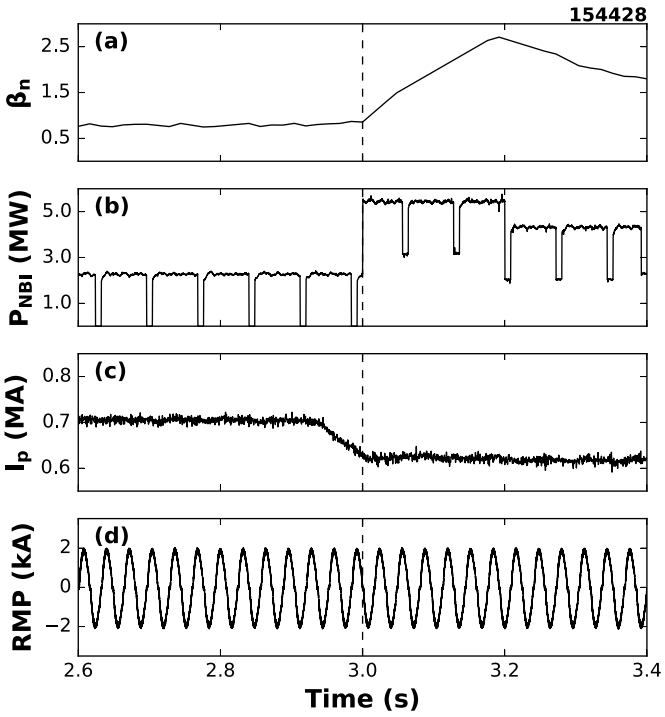

Figure 4. Example DIII-D shot parameters. The transition from L-mode to H-mode at 3 s is marked with a vertical dashed line. Time traces of β_n (*a*), NBI power (*b*), plasma current (*c*), and current for a perturbation coil (*d*) are shown. The oscillation of the coil current in (*d*) is the 25 Hz rigid rotation of the RMP.

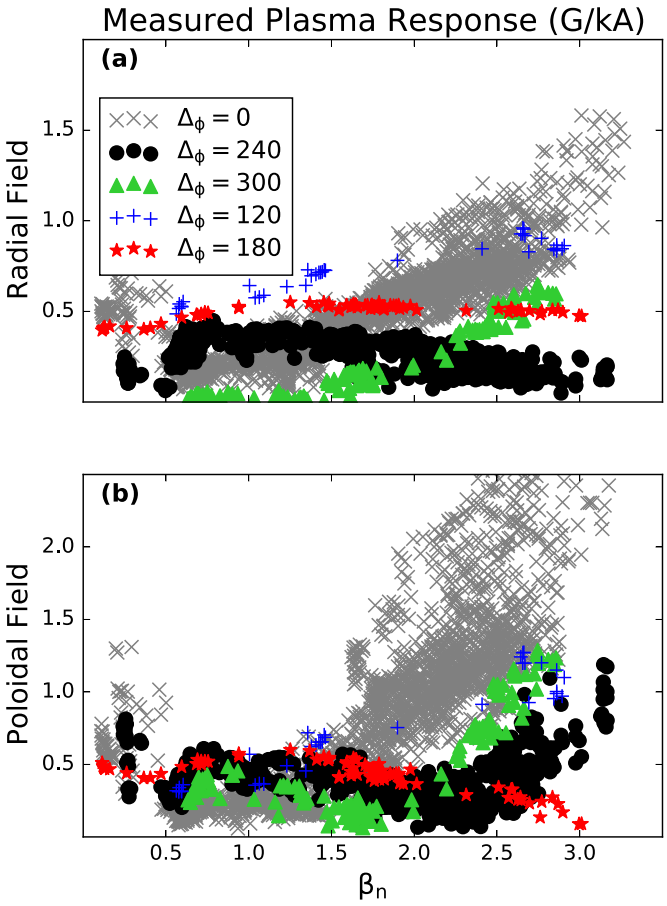

Figure 5. Measurements of the plasma response normalized to the I coil current as a function of the plasma β_n for all shots in this study. On the top (*a*) is the midplane measurement of B_r, and on the bottom (*b*) is the poloidal measurement B_p.

ion losses with a pitch angle of approximately 60° that impact the FILD. The PMTs are digitized at 1 MS s^{-1}, which allows for both a good estimate of the signal floor as well as the use of an ELM subtraction routine. Here we found all ELMs in a time slice that exceeded an amplitude threshold in the DIII-D filterscope data, and used this to determine an average ELM response of the PMTs. This was then subtracted off of the raw data prior to fitting a single $n = 1$ cosine as seen in figure 6. Each time slice with a computed plasma response was fit in several 50 ms intervals, and these were combined to determine the error of the fits.

Analysis was also done using data from a camera viewing the FILD scintillator [34]. For this purpose, the section of pixels related to NBI prompt losses was integrated for each frame. There is some difficulty in determining $\Delta F/\bar{F}$ from camera data for three reasons: First, the cameras acquire images every 7 ms, leading to greater error in measurements of the background levels when the beams are off. Second, the camera exposure time is long enough that ELM bursts cannot be easily subtracted from the data as was done with the PMTs. Lastly, while the $\Delta\phi_{UL} = 0°$ discharges could often be fit to a simple sinusoidal expression, the corresponding $\Delta\phi_{UL} = 240°$ H-mode cases had more noise. Despite these issues, camera data was available for more shots than PMT data.

As seen in figure 7, the PMT data points with smaller errors in $\Delta F/\bar{F}$ have values of $\Delta F/\bar{F}$ in the range of 0.2–0.4. There is a trend with an increase in the relative fluctuation when transitioning to H-mode for $\Delta\phi_{UL} = 240°$ even though the measured plasma response amplitude is suppressed. A weighted average of L-mode and H-mode time slices show a 62% increase in $\Delta F/\bar{F}$ for a 37% decrease in radial (see figure 7) and 50% decrease in poloidal components of the plasma response. The larger error bars associated with the H-mode fits, however, mean that this is still consistent with the L-mode and H-mode time slices having the same relative fluctuation levels, which was also found for the camera data. PMT data for the lower FILD response to counter-current injection is similarly positioned where the nearly 50% higher relative fluctuation measurement is still consistent with being equal to the co-current NBI data.

4. Orbit following simulations

4.1. Simulation setup

Simulations of four experimental time slices were run in order to better understand comparisons between cases in terms of both $\Delta\phi_{UL}$ and β_n. In order to achieve this, we choose an H-mode $\Delta\phi_{UL} = 240°$ case and a $\Delta\phi_{UL} = 0°$ slice with the same β_n value. We also choose an L-mode and H-mode time

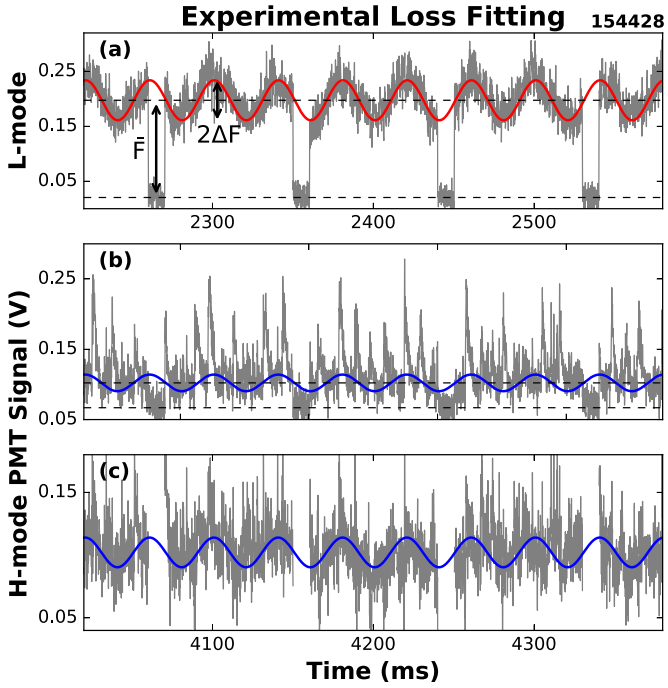

Figure 6. Example fits to experimental FILD data. The L-mode data (*a*) also shows the graphical measurements of ΔF and $\bar{F}$. H-mode data is shown before (*b*) and after (*c*) ELM subtraction. The signal is masked in (*c*) where the probing beam was turned off, as was done when fitting the fluctuations.

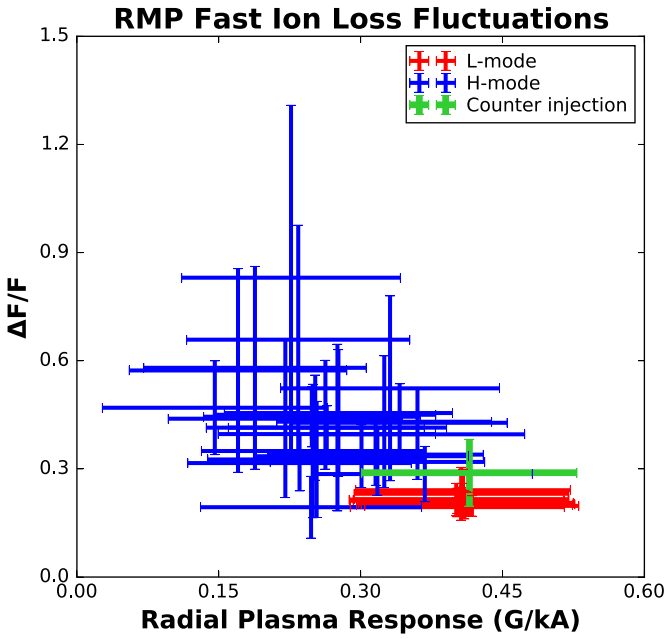

Figure 7. Fits of relative fluctuation levels in fast ion losses, $\Delta F/\bar{F}$, as a function of measured plasma response for $\Delta\phi_{\mathrm{UL}} = 240°$ across L-mode and H-mode.

slice from the $\Delta\phi_{\mathrm{UL}} = 240°$ shot with the best PMT data to compare the effects of β_n. A fifth simulation for the counter-current NBI case in L-mode was also run.

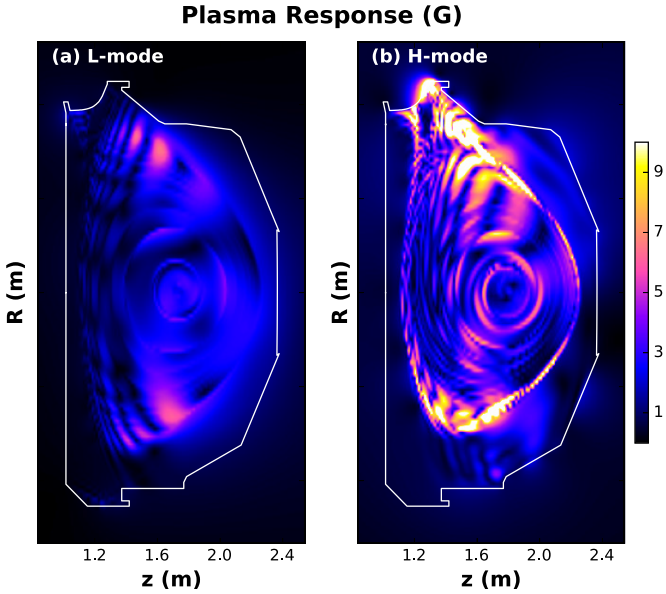

Figure 8. Calculated total magnitude of plasma response for (*a*) L-mode plasma and (*b*) H-mode plasma with $\Delta\phi_{\mathrm{UL}} = 240°$.

Magnetic fields from the MPs were simulated using a single-fluid, resistive M3D-C1 run [36]. To ensure reconstruction of the complicated effect on fast ion losses in the $\Delta\phi_{\mathrm{UL}} = 240°$ case, we attempted to recreate the physical step function of the six physical I coils in the upper and lower sets with the first five nonzero components in the Fourier decomposition. Results show that the plasma response to the I coil currents is strongest at the plasma edge near the top and bottom of the plasma as seen in figure 8. This pattern is seen across all simulations, with the main noticeable difference between high and low β_n being that higher β_n leads to a sharper edge.

These 3D fields were used as inputs into orbit following code ASCOT5 [37]. These simulations were initialized with markers from a beam deposition distribution, and markers were terminated after a full poloidal orbit to ensure a comparison between prompt beam losses in simulation and experiment. The importance of E_r in MP induced losses [22] led us to include the radial electric field in these simulations. The electric field was calculated using ion pressure and rotation data from the charge exchange recombination diagnostic. The H-mode discharges simulated here had E_r wells with magnitudes of 9–12 kV m^{-1}. All of these simulations were first carried out in ASCOT5 with only 2D equilibrium fields prior to inclusion of the MPs and plasma response in order to distinguish 2D losses from MP induced losses. The simulations used a 3D model of the DIII-D inner wall and had a 3D model of the FILD inserted at the experimental locations.

4.2. Simulation results

We find that the simulations have many similarities across all co-injection NBI results. Each of the cases shows that the fast ions lost to the MPs hit the wall in midplane diagnostic ports (see figure 9). Equilibrium field losses that are altered by the

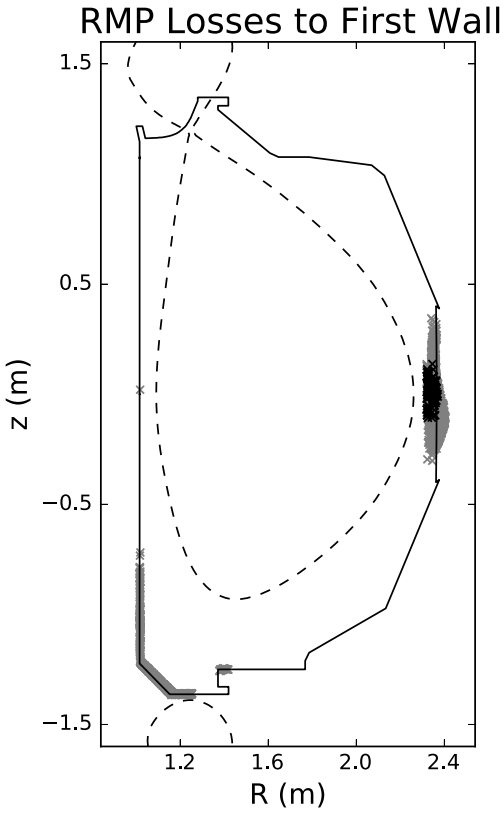

Figure 9. Location of neutral beam losses to DIII-D vessel walls due to inclusion of MPs in ASCOT5 simulations. Grey markers are ions that would be lost in equilibrium fields, but the perturbations shift where they impact the vessel wall. Black markers correspond to ions that are confined in equilibrium fields, only being lost due to the applied perturbation.

MPs are found in several main areas for co-current NBI: midplane ports, the lower diverter, and the inner wall at the midplane. A small number of losses were found to hit the vessel ceiling in a few H-mode simulations. Counter-current injection saw losses across the entire vessel floor up to the midplane ports. In both cases, ions that would have remained completely confined in the equilibrium fields only impact the first wall at the outer midplane once MPs are included.

The ionization locations of midplane losses are also similar for the different $\Delta\phi_{\mathrm{UL}}$ and β_n simulations, as shown in figure 10. Midplane losses originate as either trapped particles born outside the LCFS on the low-field side, or as passing particles born just inside the LCFS on the high-field side. The trapped particles hit the wall with pitches centered around $v_{\|}/v \approx 0.6$ which is consistent with the 60° pitch angle measured by the FILDs. The passing particles have a pitch close to 1, and are outside the range of pitch that the FILDs can accept experimentally [34]. Losses in counter-injection are born near the trapped-passing boundary for ions hitting the midplane and the lower FILD.

If we look at the ionization density scale lengths at the birth locations of losses in our ASCOT simulations, we find the experimental values of $\Delta F/\bar{F}$ give the radial displacement sizes in table 1. In the first two rows of table 1, we compare two shots with different MP poloidal spectra where we have

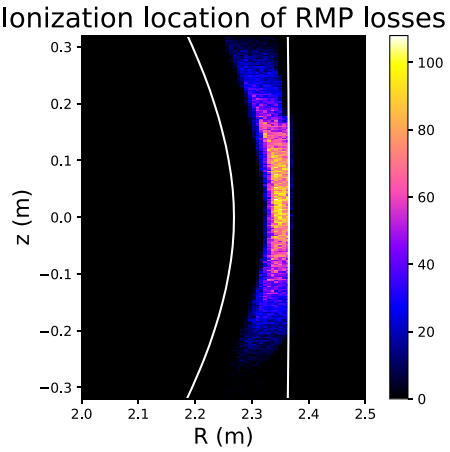

Figure 10. Ionization location of trapped neutral beam ions lost to the midplane port area of DIII-D in ASCOT5 simulations due to 3D MPs. The LCFS and innermost limiting surface of the outer wall are shown in white.

FILD camera data. The last two rows compare the L-mode and H-mode sections of a single plasma discharge using PMT data. In columns one and two, the phase difference between the MP coil sets and the normalized pressure show where each time slice falls in figure 5. Column 3 lists the fluctuation levels measured by the midplane FILD during experiment (see figure 6). The values of the density scale length in column 4 are taken at the ionization locations of ions lost in the ASCOT simulations. These two columns are input into equation (1) to calculate the experimental orbit displacements in column 5. For comparison, the orbit displacements found in ASCOT simulations are listed in column 6.

The simulated results are consistent with the calculations of the experimental displacements. It should be noted that even though the experimental calculations of the orbital displacement for the ions hitting the midplane FILD shows the L-mode case to be the lowest by about 1 cm, the simulated radial displacement is higher than the simulated H-mode section of the same discharge. The experimental errors, however, mean that these results are still consistent with each other. More importantly, the displacements for H-mode plasmas are similar in both MP spectra.

While recent simulations on ASDEX Upgrade showed that the altered pedestal density profile due to MPs had a significant effect on the fast ion losses [27], here we have not considered any effect of the edge density perturbation. Previous work on $n = 2$ MPs at DIII-D [10, 11] has looked into this in detail. There, simulations showed that changes due to the density fluctuations were within the noise levels of the simulations. This is because the birth locations are outside the highest density gradient of the pedestal in co-injection and well inside the LCFS for counter-injection.

Data from the rotation of the simulated MPs shows a clear $n = 1$ component to the midplane losses for all simulations (see figure 11), including shot 159 252, where the experiment showed a complicated suppression of the magnetic response. Figure 11 compares the ASCOT simulations of MP rotation to the experimental FILD measurements. The dependence of

Table 1. Comparison of simulated and experimental kick sizes for co-injection losses to the midplane FILD on DIII-D.

DIII-D Shot	$\Delta\phi_{\mathrm{UL}}$	β_n	$\Delta F/\bar{F}$	L_n	ξ_{expt}	ξ_{sim}
163165 (H-mode)	0°	1.9	0.31	14.4 cm	5.8 ± 1.4 cm	4.5 cm
159252 (H-mode)	240°	2.2	0.35	17.3 cm	6.0 ± 1.8 cm	4.1 cm
154428 (L-mode)	240°	0.8	0.21 ± 0.03	16.9 cm	3.5 ± 0.5 cm	4.1 cm
154428 (H-mode)	240°	1.8	0.29 ± 0.07	15.8 cm	4.6 ± 1.1 cm	3.5 cm

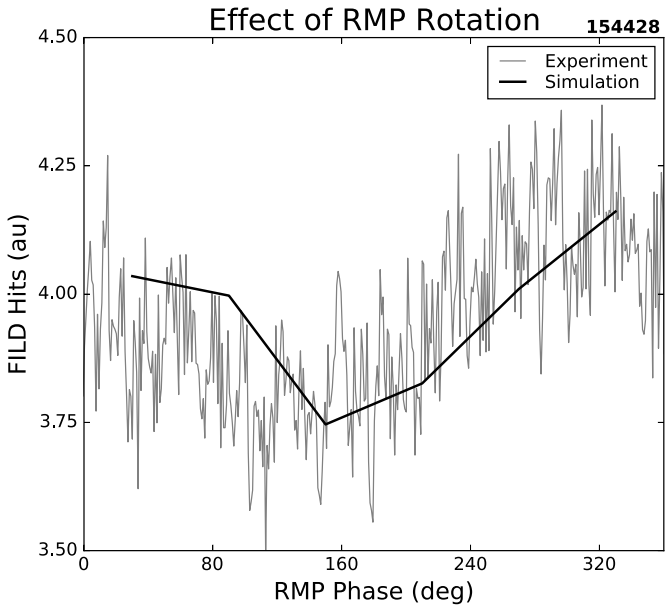

Figure 11. Comparison of fast ion losses to MP rotation in ASCOT for L-mode 240° case. Simulated losses are normalized to the experimental PMT signals during the time of interest.

losses on the phase of the MPs input into the simulation agree very well with experimental measurements.

5. Conclusion

Here we have looked at the effects of MP spectrum and β_n on fast ion losses via the LIBP technique. This allows prompt loss measurements from a FILD to be converted into the radial displacement of lost fast ions due to a MP. Simulations of these plasmas can then be used to compare theory and experiment directly.

Measurements of the plasma response were taken over a wide range of β_n for several MP spectra allowing us to use β_n as a proxy for plasma response. The MP spectrum was found to have a strong effect on the relationship between plasma response and β_n, with an enhancement of the plasma response being strongest near $\Delta_{\phi\mathrm{UL}} = 0°$, and suppression when the upper and lower applied fields were sufficiently out of phase. Suppression of the poloidal component only continues into the highest β_n for the $\Delta_{\phi\mathrm{UL}} = 180°$ case, while the radial component remains suppressed for other MP spectra.

Even with this complicated dependence of plasma response on β_n, the birth locations of co-injected fast ion losses on DIII-D have similar birth locations regardless of β_n and the plasma response amplitude. This is consistent with EAST simulation results which suggest the plasma response's suppression of magnetic islands is counteracted by the large orbit sizes of fast ions [26], allowing energetic particles to be lost over a wider range of response amplitudes.

The birth locations on DIII-D being in the scrape-off layer agree with work done on AUG [24], where resonant losses were found to be born just outside the separatrix, although the radial displacements on DIII-D are calculated to be a few centimeters larger. While these losses are all born outside the separatrix, the trapped orbits pass though the edge of the plasma on their inner leg, where the plasma response is strongest (see figures 1(*b*) and 8). Fast ions that are transported to the edge will also be subjected to this radial kick, leading to larger delayed losses. This is not constrained to energetic particles born from NBI, but would also apply to fast ions from wave heating and fusion products.

We also show that the losses induced by $n = 1$ MPs on DIII-D hit the vessel wall in a concentrated area in the midplane diagnostic ports. Equilibrium losses that are shifted by the MPs are also heavily concentrated here. The next largest group of shifted losses is in the lower divertor for co-injection, and on the vessel floor for counter-injection. The loss patterns here are reminiscent of results from EAST, where the MP losses have strong concentrations in the lower divertor and the outer midplane [26]. The midplane losses have the potential to be more damaging than the others as both co- and counter-current NBI led to increased losses at this poloidal location. In current and near-term devices, this area is also used for diagnostics, which can be more susceptible to damage.

Our experimental data and simulation results show that while β_n and MP spectra can have a significant effect on the plasma response, this does not always lead to a significant change in the average radial displacement of fast ions. The prompt loss nature of the fast ions looked at in this paper also suggest the potential for further losses induced by the applied perturbation for energetic particles transported to the plasma edge. Furthermore, we find that the losses are expected to be heavily concentrated in one of the most vulnerable areas of research devices. This suggests that diligence is required in predicting losses in future reactors, and realistic fields must be used to get accurate results.

Acknowledgments

This material is based upon work supported by the U.S. Department of Energy, Office of Science, Office of Fusion Energy Sciences, using the DIII-D National Fusion Facility,

a DOE Office of Science user facility, under Award(s) DE-FC02-04ER54698, DE-SC0020337 and Spanish Ministry of Science and Innovation under FJC2019-041002-I.

We would like to thank the DIII-D team for their support. We also thank Konsta Särkimäki and Antti Snicker for their help in setting up ASCOT5.

Disclaimer

ORCID iDs

K.R. Gage https://orcid.org/0000-0003-0262-416X
X. Chen https://orcid.org/0000-0002-8718-6877
M. Van Zeeland https://orcid.org/0000-0002-7911-2739
W.W. Heidbrink https://orcid.org/0000-0002-6942-8043
J. Hanson https://orcid.org/0000-0003-2432-4870
B. Lyons https://orcid.org/0000-0003-3232-1581
J. Galdon-Quiroga https://orcid.org/0000-0002-7415-1894
M. Garcia-Munoz https://orcid.org/0000-0002-3241-502X

References

[1] Hughes J.W., Howard N.T., Rodriguez-Fernandez P., Creely A.J., Kuang A.Q., Snyder P.B., Wilks T.M., Sweeney R. and Greenwald M. 2020 *J. Plasma Phys.* **86** 865860504
[2] Wenninger R. *et al* 2014 *Nucl. Fusion* **54** 114003
[3] Loarte A. *et al* 2003 *J. Nucl. Mater.* **313-316** 962–6
[4] Evans T.E. 2015 *Plasma Phys. Control. Fusion* **57** 123001
[5] Evans T.E. *et al* 2006 *Nat. Phys.* **2** 419–23
[6] Suttrop W. *et al* 2018 *Nucl. Fusion* **58** 096031
[7] Sun Y. *et al* 2016 *Phys. Rev. Lett.* **117** 115001
[8] Park J.-K. *et al* 2018 *Nat. Phys.* **14** 1223–8
[9] Evans T. 2013 *J. Nucl. Mater.* **438** S11–S18
[10] Van Zeeland M.A. *et al* 2013 *Plasma Phys. Control. Fusion* **56** 015009
[11] Van Zeeland M. *et al* 2015 *Nucl. Fusion* **55** 073028
[12] Garcia-Munoz M. *et al* 2013 *Plasma Phys. Control. Fusion* **55** 124014
[13] Kim K., Jhang H., Kim J. and Rhee T. 2018 *Phys. Plasmas* **25** 122511
[14] McClements K.G., Tani K., Akers R.J., Liu Y.Q., Shinohara K., Tsutsui H. and Tsuji-Iio S. 2018 *Plasma Phys. Control. Fusion* **60** 095005
[15] McClements K.G. *et al* 2015 *Plasma Phys. Control. Fusion* **57** 075003
[16] Varje J. *et al* 2016 *Nucl. Fusion* **56** 046014
[17] Särkimäki K., Varje J., Bécoulet M., Liu Y. and Kurki-Suonio T. 2018 *Nucl. Fusion* **58** 076021
[18] Sanchis L. *et al* 2021 *Nucl. Fusion* **61** 046006
[19] Kurki-Suonio T. *et al* 2016 *Plasma Phys. Control. Fusion* **59** 014013
[20] Scott S.D., Kramer G.J., Tolman E.A., Snicker A., Varje J., Särkimäki K., Wright J.C. and Rodriguez-Fernandez P. 2020 *J. Plasma Phys.* **86** 865860508
[21] Pfefferlé D., Misev C., Cooper W.A. and Graves J.P. 2014 *Nucl. Fusion* **55** 012001
[22] Huang H. and Wang L. 2020 *Plasma Sci. Technol.* **22** 105101
[23] Mou M., Wang Z., Wu N., Chen S. and Tang C. 2017 *Nucl. Fusion* **57** 046023
[24] Sanchis L. *et al* 2018 *Plasma Phys. Control. Fusion* **61** 014038
[25] Shinohara K., Suzuki Y., Kim J., Kim J.Y., Jeon Y.M., Bierwage A. and Rhee T. 2016 *Nucl. Fusion* **56** 112018
[26] He K., Sun Y., Wan B., Gu S., Jia M. and Hu Y. 2020 *Nucl. Fusion* **61** 016009
[27] Galdon-Quiroga J. *et al* (The ASDEX Upgrade Team and The EUROfusion MST1 Team) 2022 *Nucl. Fusion* **62** 096004
[28] Logan N.C., Paz-Soldan C., Park J.-K. and Nazikian R. 2016 *Phys. Plasmas* **23** 056110
[29] Reimerdes H., Chu M.S., Garofalo A.M., Jackson G.L., La Haye R.J., Navratil G.A., Okabayashi M., Scoville J.T. and Strait E.J. 2004 *Phys. Rev. Lett.* **93** 135002
[30] Chen X., Heidbrink W., Kramer G., Van Zeeland M., Austin M., Fisher R., Nazikian R., Pace D. and Petty C. 2013 *Nucl. Fusion* **53** 123019
[31] Strait E.J. 2006 *Rev. Sci. Instrum.* **77** 023502
[32] Hanson J.M., Reimerdes H., Lanctot M.J., In Y., Haye R.J.L., Jackson G.L., Navratil G.A., Okabayashi M., Sieck P.E. and Strait E.J. 2011 *Nucl. Fusion* **52** 013003
[33] Fisher R.K., Pace D.C., García-Muñoz M., Heidbrink W.W., Muscatello C.M., Van Zeeland M.A. and Zhu Y.B. 2010 *Rev. Sci. Instrum.* **81** 10D307
[34] Chen X., Fisher R.K., Pace D.C., García-Muñoz M., Chavez J.A., Heidbrink W.W. and Van Zeeland M.A. 2012 *Rev. Sci. Instrum.* **83** 10D707
[35] Chen X. *et al* 2014 *Rev. Sci. Instrum.* **85** 11E701
[36] Ferraro N.M. 2012 *Phys. Plasmas* **19** 056105
[37] Varje J., Särkimäki K., Kontula J., Ollus P., Kurki-Suonio T., Snicker A., Hirvijoki E. and Äkäslompolo S. 2019 High-performance orbit-following code ASCOT5 for Monte Carlo simulations in fusion plasmas (arXiv:1908.02482)